crystals

MDPI

Article

Constitutive Equation for Flow Stress in Superalloy 718 by Inverse Analysis under Hot Forming in a Region of Precipitation

Hyung-Won Park [1,*], Sosei Kakiuchi [2], Kyunghyun Kim [2], Akira Yanagida [3] and Jun Yanagimoto [2]

1 Faculty of Production Systems Engineering and Sciences, Komatsu University, Nu-1-3 Shichōmachi, Komatsu, Ishikawa 923-8511, Japan
2 Department of Mechanical Engineering, The University of Tokyo, Hongo 7-3-1, Bunkyo-ku, Tokyo 113-8656, Japan; evtm37@gmail.com (S.K.); kkhpnu96@gmail.com (K.K.); jun.52074.yanagimoto@cem.t.u-tokyo.ac.jp (J.Y.)
3 Department of Advanced Machinery Engineering, School of Engineering, Tokyo Denki University, 5 Senju-Asahi-cho, Adachi-ku, Tokyo 120-8551, Japan; yanagida@mail.dendai.ac.jp
* Correspondence: hyungwon.park@komatsu-u.ac.jp

Abstract: The purpose of this study is to obtain a constitutive equation of high-accuracy flow stress in superalloy 718, which allows fabrication of highly reliable disks for gas turbine engines. Hot compression tests using superalloy 718 at deformation temperatures from 850 to 1100 °C, a 67% height reduction, and strain rates of 1, 10, and 25 s^{-1} were performed to investigate the flow stress behavior, which excludes environmental effects during hot working by inverse analysis. The effects of dynamic recrystallization and strain-induced dynamic precipitation on the flow stress were also investigated. The dynamically precipitated δ phases deformed at 1050 °C and γ'' phases deformed at 950 °C might affect the increase in the plastic modulus F_1 and the decrease in the critical strain ε_c, deteriorating the accuracy of regression in terms of, for example, the strain rate sensitivity m and the temperature sensitivity A. A constitutive equation for a generalized flow curve for superalloy 718 is proposed by considering these effects.

Keywords: nickel-based superalloy; flow stress; constitutive equation; dynamic precipitation; hot working

check for updates

Citation: Park, H.-W.; Kakiuchi, S.; Kim, K.; Yanagida, A.; Yanagimoto, J. Constitutive Equation for Flow Stress in Superalloy 718 by Inverse Analysis under Hot Forming in a Region of Precipitation. *Crystals* **2021**, *11*, 811. https://doi.org/10.3390/cryst11070811

Academic Editors: Nobufumi Ueshima, Jovana Ruzic, Hongzhi Cui and Ikumu Watanabe

Received: 30 May 2021
Accepted: 4 July 2021
Published: 12 July 2021

1. Introduction

As an aircraft engine component, gas turbine disks with a gear shape are exposed to temperatures up to 650 °C at the outer periphery, a high rotation speed of about 10,500 rpm, and a load of more than 1000 MPa at the inner periphery at takeoff. Therefore, the disks should have high performance characteristics such as tensile strength at elevated temperatures, creep properties, low-cycle fatigue, and crack propagation resistance [1]. To satisfy these critical characteristics, the hot forging and heat treatment in Ni-based superalloys such as superalloy 718 have been applied in manufacturing gas turbine disks [2–4]. In the manufacture of large parts using an ultralarge forging press machine, the process prediction using computer-aided engineering (CAE) is applied to estimate the deformation behavior of a material during load, temperature, and microstructural evolution with mechanical properties [5], because there are not only cost problems such as the use of expensive materials and molds, but also a precise forging process at elevated temperatures is required to obtain heat-resistant products through microstructural control. Thus, a high-accuracy formulation of flow stress is critical for predicting the high-precision forging load by CAE, which consists of functions of stress, strain, strain rate, and temperature. Various experiments have been carried out to obtain the constitutive equation of flow stress in Ni-based superalloys at elevated temperatures and various strain rates [6–10]. However, experimental results may include the effects of internal–external heat transfer, friction, and heat generated by deformation during hot working, leading to heterogeneous deformation. The effects should be compensated prior to determining the flow stress by inverse analysis (IA) coupled with thermomechanical CAE [11,12]. To achieve a uniaxial flow stress, for which these affects are compensated, a variety of studies have been carried out by this approach using Cr–Mo–V [13], carbon [14,15] and stainless [16,17] steels, an aluminum alloy [18,19], and a nickel-based superalloy [20].

By referring to the precipitation–temperature–time (PTT) diagram for superalloy 718 [21], we can infer that gamma double prime (γ''), gamma single prime (γ'), and delta (δ) phases can be precipitated in the temperature range from about 700 to 1050 °C. Generally, the microsized δ phase in block and needle shapes precipitate mainly at grain boundaries, suppressing grain growth at elevated temperatures [22,23]. Nanosized γ'' phases with an elongated disk shape and γ' phases with a spheroidal shape precipitate primarily in grains, increasing the strength of the material [24,25]. Hence, a solid-solution treatment at about 950 °C for 1 h and a two-step aging treatment at about 720 °C for 8 h for the first step and about 620 °C for 10 h for the second step was performed to precipitate both γ'' and γ' phases in the matrix [4]. Strain-induced dynamic precipitation (SIDP) may occur, when the strain is applied to precipitate hardenable metals during hot working under specific conditions [26–28]. Precipitation strengthening or softening is induced by dynamic precipitation under working condition and then dynamic precipitation changes the flow stress during hot working [28–31]. Accordingly, it is essential to investigate the effects of SIDP on flow stress in superalloy 718 in the temperature range from about 700 to 1050 °C. Dynamic recrystallized ultrafine grains in superalloy 718 were formed with high strength after compression at temperatures from 900 to 1050 °C and strain rates from 0.001 to 10 s^{-1} [9]. Furthermore, most of the studies on the flow stress have been carried out at strain rates lower than 10 s^{-1} [6–9,27]. However, to contribute to productivity improvement, it is important to investigate the flow stress behavior at strain rates higher than 10 s^{-1}.

The purpose of this study is to obtain a constitutive equation of the high-accuracy flow stress in superalloy 718, which allows fabrication of highly reliable disks of gas turbine engines. Hot compression tests using superalloy 718 at deformation temperatures from 850 to 1100 °C, a 67% height reduction, and strain rates of 1, 10, and 25 s^{-1} were performed to investigate the flow stress behavior including dynamic recrystallization (DRX) and SIDP. The constitutive equation of this behavior was obtained.

2. Materials and Methods

2.1. Materials

In this study, superalloy 718 was subjected to a solid-solution treatment for 2 h at 1070 °C, which is higher than the delta solvus, to dissolve δ phases into the matrix. It was then machined into specimens of two sizes, 8 mm diameter × 12 mm height and 6 mm diameter × 9 mm height, for hot compression tests. The microstructure of the solid-solution-treated superalloy 718 with an average grain size of approximately 21 μm showed equiaxed grains with twins; a few microsized δ phases remained around the grain boundary, as shown in Figure 1. Its chemical composition is shown in Table 1.

Table 1. Chemical composition of superalloy 718 (mass%).

Ni	Cr	Nb	Ti	Al	Co	Mn	Cu	C	Si	B	Fe
52.4	18.4	5.37	0.99	0.60	0.24	0.06	0.06	0.03	0.06	0.004	Bal.

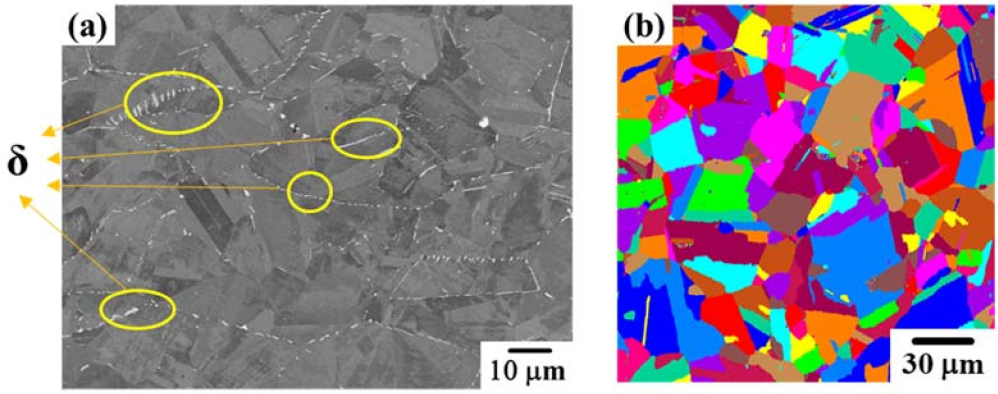

Figure 1. Microstructure of solid-solution-treated superalloy 718 with an average grain size of approximately 21 μm: (**a**) FE–SEM image and (**b**) unique grain map ($\theta < 15°$).

2.2. Hot Compression Tests and Microstructural Observation

Fifteen ton and five ton high-speed compression-testing machines (ThermecMastor-Z, Fuji Electronic Industrial Co., Ltd., Tsurugashima, Japan) were used in this test. Hot compression tests were performed to obtain load–stroke data at deformation temperatures from 850 to 1100 °C, a 67% height reduction (an average strain of 1.1), and strain rates of 1, 10, and 25 s^{-1}. The 15-ton compression-testing machine was used at deformation temperatures from 900 to 1100 °C using a specimen of 8 mm diameter × 12 mm height. The 5-ton compression-testing machine was used only at a deformation temperature of 850 °C using a specimen of 6 mm diameter × 9 mm height.

Mica sheets were placed between the dies and the specimen to reduce both the friction and heat transfer to the dies. Nitrogen gas was used as an inert atmosphere to prevent the oxidation of the specimen at elevated temperatures. The specimen was induction-heated at a constant rate of 10 °C s^{-1} up to the target temperature and then held at this temperature for 3 min to homogenize the temperature distribution. Afterward, the specimen was compressed to 67% height reduction and then water-quenched to freeze the microstructure. The compression test profile of temperature vs. time is shown in Figure 2.

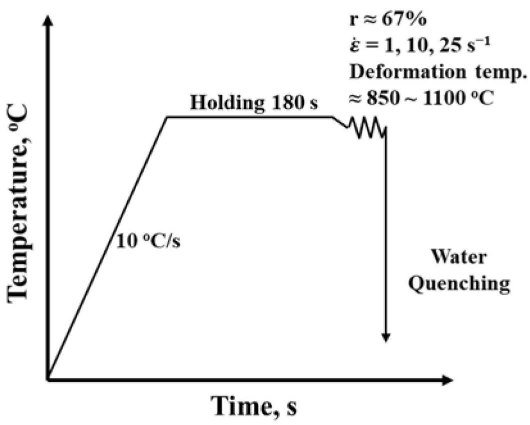

Figure 2. Compression test profile of temperature vs. time.

To investigate the microstructures of the test specimens, the specimens were cut in half along their compression axis before and after the hot compression tests. The cut specimens were mechanically polished with abrasive paper and 0.04 μm OP-U nondrying colloidal silica suspension. They were then characterized by field-emission scanning electron microscopy (FE–SEM, JEOL 7100F) electron backscattering diffraction (EBSD) analysis.

2.3. Flow Curve Determination by Inverse Analysis Coupled with Thermomechanical CAE

The constitutive equation for the flow curve used in IA was proposed by Yanagida et al. [11], where the softening phenomena such as dynamic recovery (DRV) and DRX during deformation were taken into account. The equation is expressed as

$$\begin{cases} \overline{\sigma} = F_1\overline{\varepsilon}^n & (\overline{\varepsilon} \leq \varepsilon_c) \\ \overline{\sigma} = F_2 \exp\left[a(\overline{\varepsilon} - \varepsilon_{max})^2\right] + F_3 & (\overline{\varepsilon} \geq \varepsilon_c) \end{cases}, \tag{1}$$

$$F_2 = \frac{F_1{\varepsilon_c}^n - F_3}{\exp\left[a(\varepsilon_c - \varepsilon_{max})^2\right]}, \tag{2}$$

$$a = \frac{nF_1{\varepsilon_c}^{n-1}}{2(\varepsilon_c - \varepsilon_{max})(F_1{\varepsilon_c}^n - F_3)}, \tag{3}$$

$$\varepsilon_{max} = \varepsilon_c + \frac{F_1{\varepsilon_c}^n - F_3}{nF_1{\varepsilon_c}^{n-1} - (n-1){\varepsilon_c}^{-1}(F_1{\varepsilon_c}^n - F_3)}, \tag{4}$$

$$\sigma_f = \overline{\sigma}\cdot\dot{\varepsilon}^{m_0}, \tag{5}$$

where F_1 (plastic modulus), n (work hardening exponent), ε_c (critical strain), ε_{max} (strain at peak stress), and F_3 (steady-state stress) are independent parameters that can be obtained by IA, and all are material constants with clear individual physical meanings. Moreover, F_2, a, and ε_{max} are dependent parameters when full dynamic recrystallization occurs during deformation and continuity of the stress condition and its first- and second-order derivatives at ε_c are applied.

The distributed internal temperature used in IA is calculated as

$$\rho c\left(\frac{\partial T}{\partial t} - v_r\frac{\partial T}{\partial r}\right) = \frac{\kappa}{r}\left(r\frac{\partial^2 T}{\partial r^2} - \frac{\partial^2 T}{\partial z}\right) + \dot{Q}, \tag{6}$$

$$\dot{Q} = \sigma_f\dot{\varepsilon} + \dot{q}_e, \tag{7}$$

where ρ, c, κ, and $\dot{Q}$ are the density, specific heat, thermal conductivity, and amount of internal heat generated, respectively; $\sigma_f\dot{\varepsilon}$ is the amount of internal heat generated by plastic work, and $\dot{q}_e$ is the amount of internal heat generated by the electromagnetic factor of induction heating. As can be seen from Equation (7), a high flow stress and a high strain rate can lead to greater internal heat generation.

The flow stress $\overline{\sigma}$ in Equation (1) is obtained below, taking T_0 as the reference temperature corresponding to the initial testing temperature:

$$\overline{\sigma}|_T = \overline{\sigma}|_{T_0}\frac{\exp(A_0/T)}{\exp(A_0/T_0)} \tag{8}$$

By using $\overline{\sigma}|_T$ in Equation (8) instead of $\overline{\sigma}$ in Equation (5), we obtain the flow curve with a compensated temperature and strain rate distribution inside the workpiece by IA, expressed as

$$\overline{\sigma}^*|_T = \overline{\sigma}|_T\cdot\dot{\varepsilon}^{m_0}, \tag{9}$$

where m_0 is the strain rate sensitivity at reference temperature T_0. From Equation (9), $\overline{\sigma}^*|_T$ represents the temperature-corrected flow stress and $\overline{\sigma}|_{T_0}$ is the stress at the reference temperature [11]. Therefore, the stress decreases at a specific point with increasing temperature. The stress was obtained before IA to determine the flow curve from the load–stroke curve of hot compression test by dividing the measured load by the cross section assuming a uniform deformation, which is here called the apparent stress. In this work, $m_0 = 0.08$ (strain rate sensitivity) and two A_0 values (temperature sensitivity), $A_0 = 7000$ or 8000, are selectively applied to reduce the remaining error in IA and to improve the accuracy of flow stress expressed by Equation (1). As a result of the parameter regression shown later in the results and discussion, there is no marked difference between this assumed value and the final one obtained, so it is considered that the change in the flow curve is small even when m_0 and A_0 are updated and regression is again performed.

The flow stress was determined by IA associated with thermomechanical–electromagnetic coupled finite element analysis (FEA), using an in-house code [12], to minimize the error between the measured load-reduction curves and the independent parameters of the flow curve determined in Equation (1). The IA performed to identify the flow curve was terminated when the error between the measured load and the calculated load became lower than the threshold determined using the least squares method (Lavenberg–Marquardt method). The final relative error in calculated loads in IA of hot compression test and experiments, which is an identification error of upsetting force in IA, lies in the 1–2.5% range, which is denoted as "error" in the rightmost column in Table 2.

Table 2. Parameters for flow stress determined by inverse analysis.

Temperature, °C	Strain Rate, s^{-1}	F_1	n	ε_c	F_3	ε_{max}	Error, %
1100	1	255.248	0.030	0.123	196.800	0.231	1.8
	10	336.008	0.111	0.217	199.017	0.388	2.0
	25	420.233	0.158	0.232	226.308	0.406	2.2
1050	1	320.102	0.036	0.119	250.717	0.219	0.7
	10	425.052	0.090	0.190	287.614	0.332	1.5
	25	532.354	0.178	0.258	302.749	0.434	1.9
1000	1	361.269	0.046	0.163	265.924	0.301	1.8
	10	512.820	0.126	0.248	308.279	0.436	1.9
	25	605.083	0.205	0.337	357.156	0.551	1.9
950	1	549.412	0.072	0.119	507.551	8.267	2.1
	10	640.235	0.134	0.302	376.275	0.533	2.4
	25	728.158	0.251	0.369	372.241	0.619	1.5
900	1	695.208	0.124	0.832	721.084	0.086	2.2
	10	836.635	0.257	0.448	585.873	0.620	1.9
	25	873.508	0.343	0.489	512.182	0.730	1.6
850	1	990.674	0.214	0.312	976.117	−14.271	1.4
	10	1098.662	0.247	0.736	908.623	0.976	2.2
	25	1210.014	0.361	0.704	983.583	0.835	2.2

3. Results and Discussion

3.1. Comparison of Flow Curves Obtained by Experiment and Inverse Analysis

Figure 3 shows flow curves obtained by experiment (dotted line) and IA (line) at deformation temperatures from 850 to 1100 °C and strain rates of 1, 10, and 25 s^{-1}. The flow curves obtained by experiment are calculated using Equation (10) and IA results are summarized in Table 2, which are used to calculate the flow stress:

$$\begin{cases} \sigma = \frac{F}{A} \cdot \frac{L_0 - \Delta L}{L_0} \\ \varepsilon = -ln\left(\frac{L_0 - \Delta L}{L_0}\right) \end{cases}, \tag{10}$$

where L_0 and A are the original height and area of the specimen before compression, and F and ΔL are the load and stroke during compression, respectively.

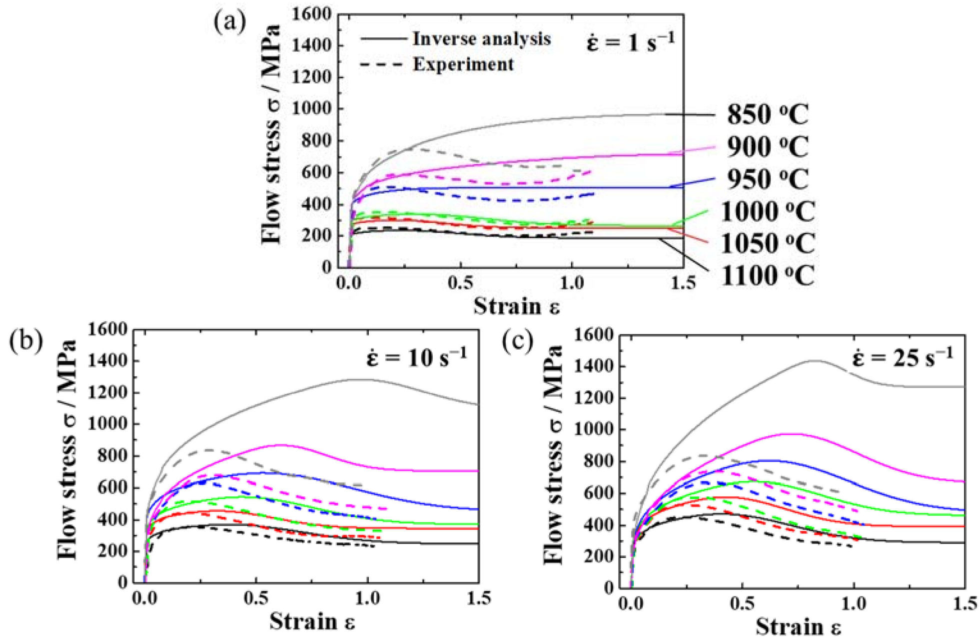

Figure 3. Flow curves obtained from experiment (dotted line) and inverse analysis (line) at deformation temperatures from 850 to 1100 °C and strain rates of (**a**) 1, (**b**) 10, and (**c**) 25 s^{-1}.

As shown in Figure 3, with decreasing deformation temperature and increasing strain rate, both flow stresses obtained by experiment and IA increase. At a strain rate of 1 s^{-1}, as shown in Figure 3a, the experimental axial flow stresses at deformation temperatures from 850 to 1100 °C represent the DRX behavior. On the other hand, the flow stresses obtained by IA show work hardening (WH) behavior at deformation temperatures of 850 and 900 °C and complex dynamic events such as WH and DRV or WH, DRV, and DRX at a deformation temperature of 950 °C. At strain rates from 1 to 25 s^{-1}, a small difference between both flow curves obtained by experiment and IA is observed at deformation temperatures above 1000 °C and strain rates below 10 s^{-1}. However, the larger difference between the curves can be observed at deformation temperatures below 1000 °C and strain rates above 10 s^{-1}. The significant differences clearly show that an unrealistic stress–strain curve will be obtained by the hot compression test and indicated by Equation (10), due to severe heterogeneous deformation, heat generated by deformation during hot working, internal–external heat transfer and induced temperature distribution inside test piece, and friction. This homogeneity may lead to low stress obtained by experiments, compared to uniaxial-flow stress at uniform temperature and strain rate identified by the IA of load–stroke curve in the experiment.

The calculated temperature distribution (1/4 axisymmetric model) of superalloy 718 compressed at a 60% height reduction, various strain rates, and deformation temperatures of 950 and 1100 °C is visualized using micro AVS® and shown in Figure 4. The figure shows that the temperature is higher at the center of the specimen and lower near the top surface. At a strain rate of 1 s^{-1} and both deformation temperatures, the temperature near the center surface (right side) is higher owing to the electromagnetic factor of induction heating rather than the heat generated by the plastic work. The temperature difference (ΔT) values between the maximum and deformation temperatures at strain rates of 1, 10, and 25 s^{-1} are 18, 95, and 120 °C at a deformation temperature of 950 °C, and the differences are 2, 60, and 81 °C at a deformation temperature of 1100 °C, respectively. ΔT increases with increasing strain rate and decreasing deformation temperature, meaning that the heat generated by the plastic work is higher.

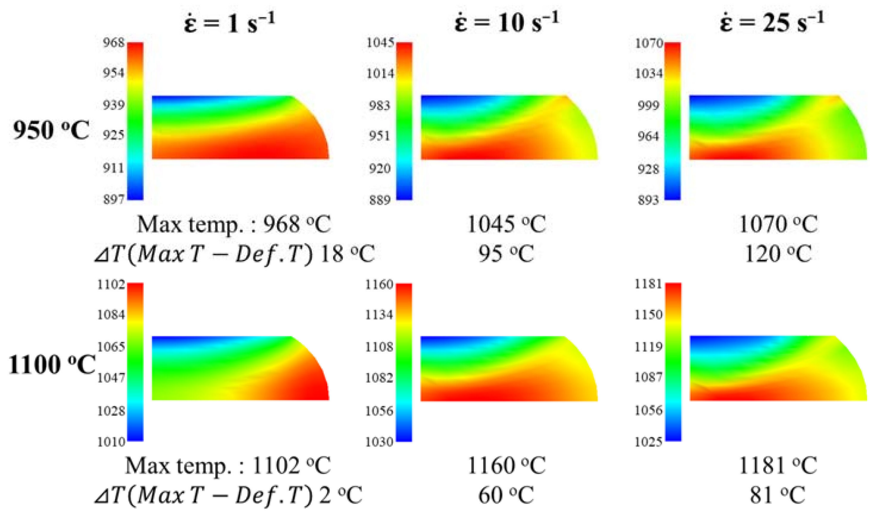

Figure 4. Temperature distribution (1/4 axisymmetric model) at deformation temperatures of 950 and 1100 °C, a 60% height reduction, and strain rates of 1, 10, and 25 s^{-1}.

The ΔT in 0.2% carbon steel compressed at a 75% height reduction, a strain rate of 200 s^{-1}, and a deformation temperature of 1000 °C was 61 °C [15]. In contrast, the ΔT in superalloy 718 compressed at a 60% height reduction, a strain rate of 25 s^{-1}, and a deformation temperature of 1100 °C was 81 °C. Despite the small height reduction, low strain rate, and high deformation temperature, the heat generated by the plastic work in superalloy 718 is larger than that in 0.2% carbon steel.

Figure 5 shows the microstructural evolution of superalloy 718, where the center of the specimen in the middle of the compression axis was observed, compressed at a 67% height reduction, deformation temperatures of 950 and 1100 °C, and strain rates of 1, 10, and 25 s^{-1}. Nonrecrystallized areas and ultrafine microstructures with an average grain size from 1 to 3 μm at a deformation temperature of 950 °C were widely observed, as shown in Figure 5a–c. In contrast, almost fully recrystallized areas and fine microstructures with an average grain size from 6 to 9 μm at a deformation temperature of 1100 °C were observed, as shown in Figure 5d–f. With increasing strain rate and deformation temperature, the grain size and DRX fraction tend to increase.

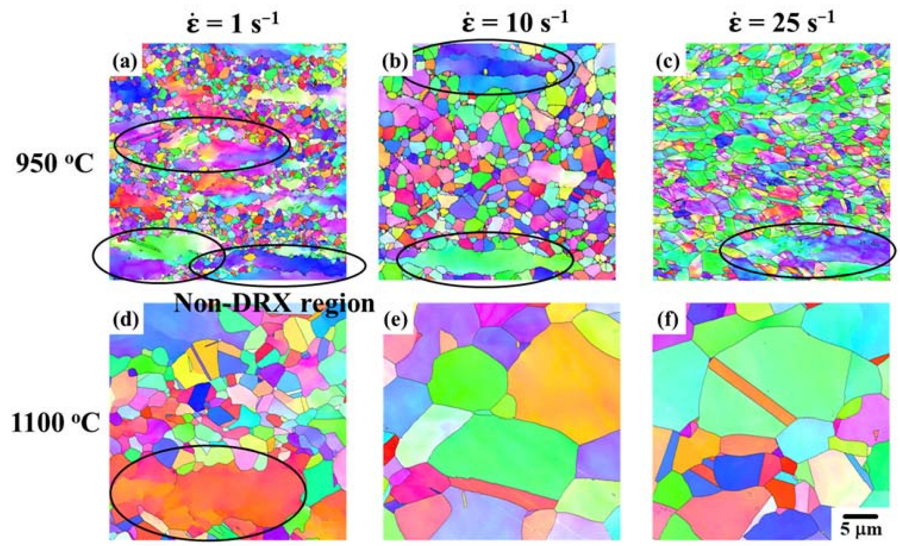

Figure 5. Microstructural evolution of superalloy 718 compressed at 67% height reduction, deformation temperatures of (**a**–**c**) 950 °C and (**d**–**f**) 1100 °C, and strain rates of (**a**,**d**) 1 s^{-1}, (**b**,**e**) 10 s^{-1}, and (**c**,**f**) 25 s^{-1}.

The flow curve obtained from the experimental results at a deformation temperature of 950 °C and a strain rate of 1 s^{-1} shows strong DRX behavior. On the other hand, the flow curve obtained from IA results at a deformation temperature of 950 °C and a strain rate of 1 s^{-1} shows complex dynamic events such as WH and DRV or WH, DRV, and DRX, as shown in Figure 3a. As noted, the experimental results used to obtain the flow curve may include the effects of internal–external heat transfer, friction, and heat generated owing to deformation during hot working, leading to the heterogeneous deformation, so that uniaxial flow stress rather than axial flow stress can be achieved. Accordingly, it seems reasonable to conclude that flow curves obtained by IA show the original flow behavior, which is the uniaxial flow curve.

3.2. Flow Curve Regression

The logarithmic relationship between the maximum stress (peak stress) of flow curves using the hyperbolic sine-law equation and the Zener–Hollomon parameter (Z) [32] is used to validate the results of IA:

$$Z = \dot{\varepsilon} \exp\left(\frac{Q_{DRX}}{RT}\right) = A'[\sinh(\alpha\overline{\sigma})]^{\,n'}, \tag{11}$$

where $\dot{\varepsilon}$ is the strain rate (s^{-1}), Q_{DRX} is the activation energy for DRX (J/mol), R is the gas constant (8.314 J/mol K), T is the deformation temperature (K), $\overline{\sigma}$ is the flow stress (MPa), and A', α, and n' are material constants. A good validity of IA results is shown in Figure 6.

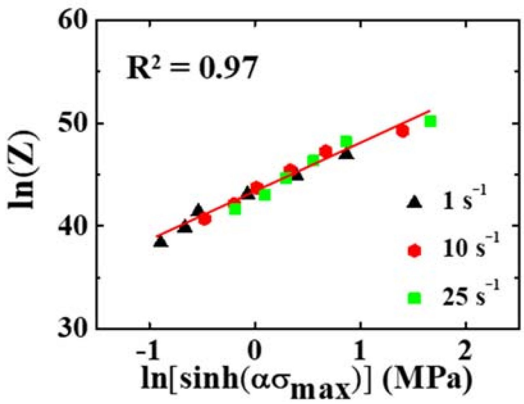

Figure 6. Hyperbolic sine function of flow stresses obtained from inverse analysis according to the Zener–Holloman parameter.

The DRX activation energy of this alloy at deformation temperatures from 850 to 1100 °C and strain rates from 1 to 25 s^{-1} was calculated to be 438.17 kJ/mol. Azarbarmas et al. [7] reported that the hot deformation activation energy of superalloy 718 at deformation temperatures from 950 to 1100 °C and strain rates from 0.001 to 10 s^{-1} was 437 kJ/mol, which was calculated using the hyperbolic sine-law equation. Hot deformation activation energies of 429–467 kJ/mol in superalloy 718 have also been reported [33,34]; these activation energies are similar to those we obtained in this investigation. In addition, Nowotnik [28] reported that the mean hot deformation activation energy in superalloy 718 compressed at a strain rate of about 10^{-4} s^{-1} and temperatures from 900 to 1150 °C was 450.8 kJ/mol and that it increased from 354 to 590 kJ/mol with decreasing deformation temperature from 1150 to 900 °C.

The relationships among the critical strain ε_c, the work hardening coefficient n, and the Z parameter are shown in Figure 7, and ε_c and n were calculated as

$$\varepsilon_c = B_1 Z^{B_2}, \tag{12}$$

$$n = B_3 \ln Z + B_4, \tag{13}$$

where B_1 is 0.00027, B_2 is 0.1569, B_3 is 0.0274, and B_4 is –1.0414; ε_c and n for non-DRX regions at deformation temperatures of 850 and 900 °C, and a strain rate of 1 s^{-1} were excluded to obtain a regression to reduce error.

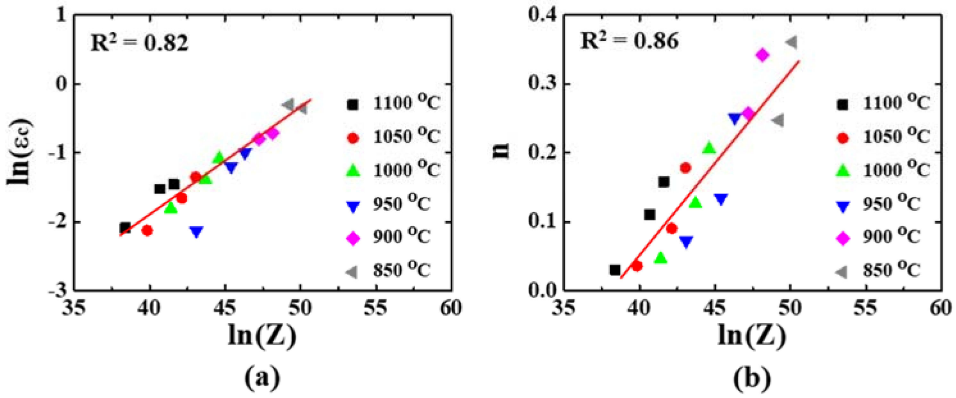

Figure 7. (**a**) Critical strain ε_c and (**b**) work hardening coefficient n according to Zener–Holloman parameter.

The strain rate sensitivity m depends on the deformation temperature, as shown in Figure 8, and is expressed by Equation (14) as

$$m = 4.32 \times 10^{-4}T - 0.4276, \tag{14}$$

where T is the deformation temperature (K).

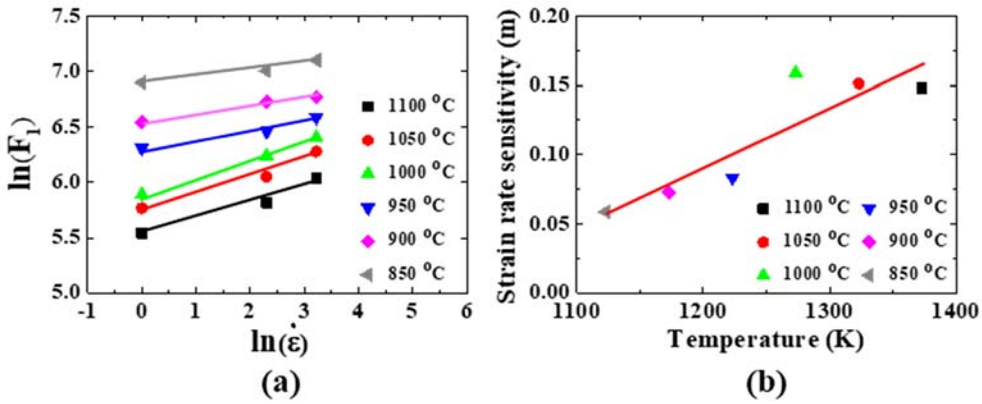

Figure 8. Strain rate sensitivity m at various temperatures calculated as (**a**) $m = \partial \ln(F_1)/\partial \ln(\dot{\varepsilon})$ and (**b**) the regression of the strain rate sensitivity m as a function of temperature.

In Figure 8a, the plastic modulus F_1 tends to a relatively significant increase with decreasing deformation temperature from 1100 to 1050 °C and from 1000 to 950 °C, diminishing the accuracy of the regression for the strain rate sensitivity, as shown in Figure 8b.

The arithmetic average of the work hardening coefficient $\overline{n}$ was used instead of the scattered n values to calculate the optimized plastic modulus F_1* [12]. The plastic modulus F_1 is modified to $F_1{}'$ using

$$\int_0^{\varepsilon_c} F_1 \overline{\varepsilon}^n d\overline{\varepsilon} = \int_0^{\varepsilon_c} F_1{}' \overline{\varepsilon}^{\overline{n}} d\overline{\varepsilon} \tag{15}$$

$$F_1' = \frac{(\overline{n}+1)F_1\varepsilon_c^n}{(n+1)\varepsilon_c^{\overline{n}}}. \tag{16}$$

The optimized plastic modulus F_1* and the optimized steady-state stress F_3* depend on the temperature. Accordingly, F_1*, and F_3* can be expressed as

$$\ln\left(F_1{}'\dot{\varepsilon}^{(m_0-m)}\right) = A\left(\frac{1}{T} - \frac{1}{T^*}\right) + \ln(F_1{}^*) \tag{17}$$

$$\ln(F_3) = A\left(\frac{1}{T} - \frac{1}{T^*}\right) + \ln(F_3{}^*), \tag{18}$$

where A is the temperature sensitivity and T* is the reference temperature.

Figure 9 shows regressions of the temperature sensitivity A regressed by $\ln\left(F_1{}'\dot{\varepsilon}^{m_0-m}\right)$ and $\ln(F_3)$ as functions of $10^3(1/T–1/T^*)$; 1223 K (950 °C) was used as the reference temperature T*. The temperature sensitivity $A1$ and the optimized plastic modulus F_1* are 5301.8 and 536.8, and the temperature sensitivity $A2$ and the optimized steady-state stress F_3* are 9108.2 and 336.8, respectively. The values of $\ln\left(F_1{}'\dot{\varepsilon}^{m_0-m}\right)$ at deformation temperatures of 950 and 1050 °C are located above the regression line of $\ln\left(F_1{}'\dot{\varepsilon}^{m_0-m}\right)$ as a function of $10^3(1/T–1/T^*)$, as shown in Figure 9a. In particular, the value at a deformation temperature of 950 °C deviates further from the regression line. This is attributed to the fact that $F_1{}'\dot{\varepsilon}^{(m_0-m)}$ at deformation temperatures of 950 and 1050 °C increases at relatively high F_1 and low ε_c values.

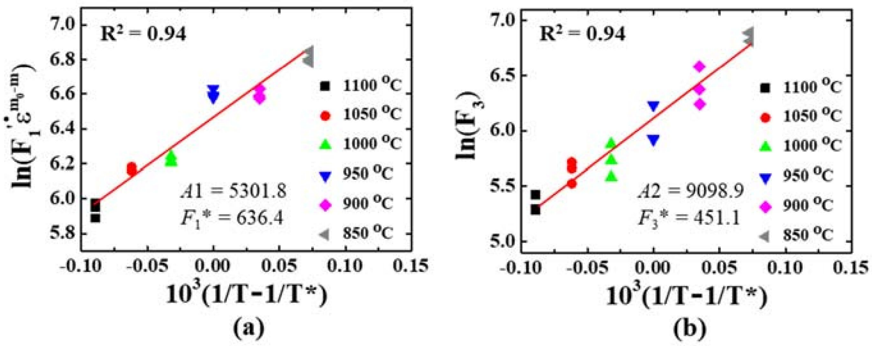

Figure 9. Temperature sensitivity A and each optimized stress regressed by (**a**) $\ln\left(F_1{}'\dot{\varepsilon}^{m_0-m}\right)$ and (**b**) $\ln(F_3)$ as functions of $10^3(1/T - 1/T^*)$ with reference temperature T* = 1223 K (950 °C).

3.3. Generalized Flow Curve

The complete formulation of the generalized flow curve can be expressed as

$$\sigma^* = \overline{\sigma}\dot{\varepsilon}^m \exp\left[A\left(\frac{1}{T} - \frac{1}{T^*}\right)\right]\left\{\begin{array}{ll} \overline{\sigma} = F_1{}^*\overline{\varepsilon}^n & (\overline{\varepsilon} < \varepsilon_c) \\ \overline{\sigma} = F_2{}^* \exp\left[a^*(\overline{\varepsilon} - \varepsilon_{max})^2\right] + F_3{}^* & (\overline{\varepsilon} \geq \varepsilon_c) \end{array}\right\}, \tag{19}$$

where m is the strain rate sensitivity, n is the work hardening coefficient, and ε_c is the critical strain. The optimized plastic modulus F_1* and the optimized steady-state stress F_3* are constant values, A is the temperature sensitivity obtained by regression, T* is the reference temperature (K), and F_2* and a* are dependent coefficients. The parameters used to obtain generalized flow curve are summarized in Table 3.

Table 3. Parameters used to obtain the generalized flow curve.

Parameters	Values or Equations
Strain rate sensitivity m	$4.32 \times 10^{-4}T - 0.4276$
Temperature sensitivity A	$A1 = 5301.8$ (comparison) $A2 = 9108.2$ (applied)
Work hardening coefficient n	$2.74 \times 10^{-2}\left\{\dot{\varepsilon}\exp\left(\frac{52{,}703}{T}\right)\right\} - 1.0414$
Critical strain ε_c	$2.67 \times 10^{-4}\left\{\dot{\varepsilon}\exp\left(\frac{52{,}703}{T}\right)\right\}^{0.1569}$
Optimized plastic modulus F_1*	636.4
Optimized steady-state stress F_3*	451.1
Reference temperature T* (K)	1223

Figure 10 shows the flow curves obtained from results of IA and the constitutive equation (CE) calculated using temperature sensitivities $A1$ and $A2$. In the case of using $A1$ to calculate CE, flow curves obtained from IA and CE results at various deformation temperatures and strain rates show inferior matching; however, when $A2$ is applied, high matching of flow curves obtained from IA and CE results can be shown. Since the formulation of the generalized flow curve is based on the dynamic softening of DRV and DRX, the flow curves obtained from IA and CE results at deformation temperatures of 900 and 850 °C and a strain rate of 1 s^{-1} show worse matching, where the flow curve obtained from results of CE calculation shows the DRX behavior, whereas the flow curve obtained from IA results shows WH behavior.

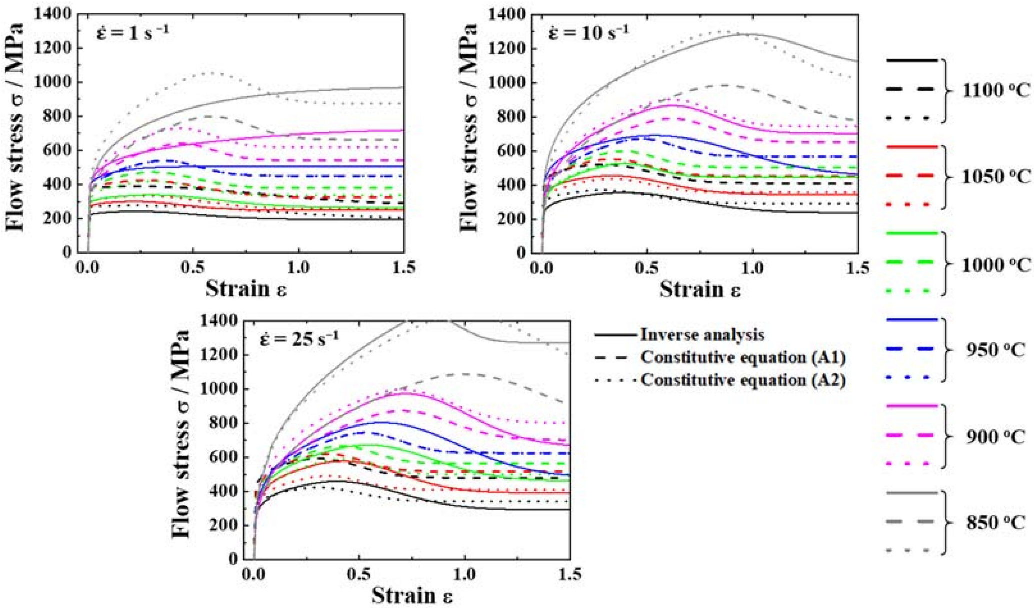

Figure 10. Flow curves obtained from results of IA and CEs calculated using temperature sensitivities $A1$ and $A2$.

To compare the flow stress correlation between IA and CEs calculated using $A1$ and $A2$ (CE($A1$) and CE($A2$), respectively), the relationship of the peak flow stress and the steady-state stress at $\varepsilon_{2.0}$ between IA and CE is shown in Figure 11. The 45° line on the x–y axis is the reference axis, and the error decreases as it converges to the reference axis. The relative error ξ can be expressed as

$$\xi = \frac{1}{N}\sum\left|\frac{\sigma_{CE} - \sigma_{IA}}{\sigma_{IA}}\right| \times 100\%. \quad (20)$$

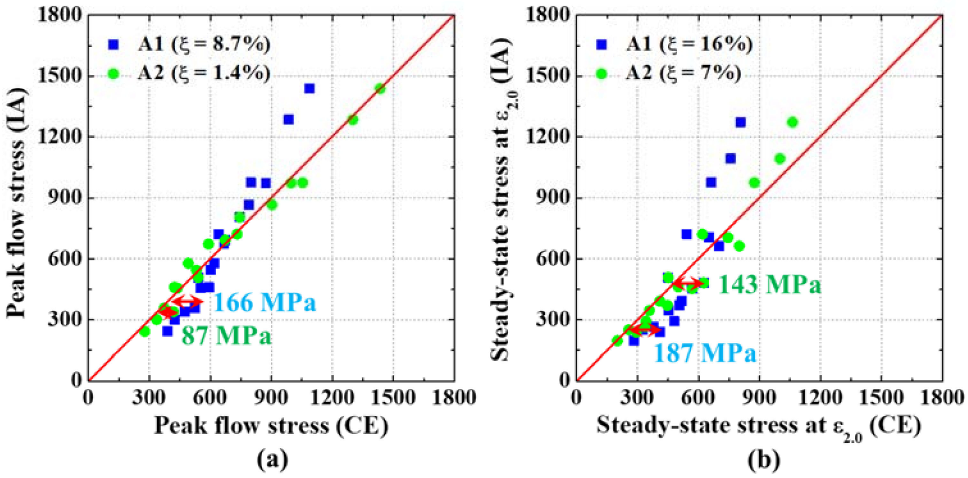

Figure 11. Flow stress correlation between IA and CEs calculated using temperature sensitivities *A*1 and *A*2: (**a**) peak flow stress and (**b**) steady-state stress at $\varepsilon_{2.0}$.

In the relationship for the peak flow stress shown in Figure 11a, except for two values for non-DRX regions at deformation temperatures of 850 and 900 °C, and a strain rate of 1 s^{-1}, the maximum difference between IA and CE(*A*1) is 166 MPa. In contrast, that between IA and CE(*A*2) is 87 MPa. Under all conditions, the relative error ξ between IA and CE(*A*1) is 8.7%; however, relative error between IA and CE(*A*2) is 1.4%. In the relationship for the steady-state stress at $\varepsilon_{2.0}$ shown in Figure 11b, except for the two values mentioned above, the maximum differences between IA and CE(*A*1), and between IA and CE(*A*2) are 187 and 143 MPa, respectively. Under all conditions, the relative error ξ values between IA and CE(*A*1), and between IA and CE(*A*2) are 16% and 7%, respectively. In the case of CE(*A*2), a higher correlation of the peak flow stress and the steady-state stress between IA and CE can be confirmed.

By referring to the PTT diagram [21], we can infer that the δ and the γ'' phases can be precipitated by holding the temperature at around 950 and 850 °C for about 10 min, respectively. Thomas et al. [21] mentioned that the PTT curve moves towards higher temperatures when the precipitation in superalloy 718 occurs concurrently with deformation. When superalloy 718 was compressed at deformation temperatures from 800 to 950 °C, a strain rate of 0.1 s^{-1}, and strains up to 0.2, the start time of precipitation in the PTT diagram decreases slightly with increasing applied deformation [26]. In 26NiCrMoV 14-5 medium carbon low alloy steel compressed at 950 °C and higher, and at low strain rates (0.01–0.1 s^{-1}), DRX precedes dynamic precipitation and decreases considerably the work hardening rate; however, at very high strain rates (1 s^{-1} and higher), dynamic precipitation is stimulated and precedes DRX; therefore, the flow curve is characterized by a high value [31]. The occurrence of precipitation is a function of solid-solution concentration, strain, temperature, and time. Accordingly, it can be considered that the PTT curve can move in any direction depending on the abovementioned condition. In this study, SIDP during hot working might be activated because of the relatively higher strain rate from 1 to 25 s^{-1}, shifting the PTT curve to the northwest side, which corresponded to both shorter times and higher temperatures. Similarly, the strain-induced dynamic transformation (SIDT) occurs during hot working [35–37].

After precipitation in the matrix, dislocations are accumulated around precipitates during deformation, resulting in an increase in stress caused by the generated stress zone near precipitates [38]. The precipitation strengthening due to coherency strains is expressed by

$$\Delta\sigma \approx 6G\varepsilon^{3/2}\sqrt{\frac{rf}{b}} \tag{21}$$

where *G* is the shear modulus, ε is the measure of the strain field, *r* is the radius of a precipitate particle, *f* is the volume fraction of the dispersed phase, and *b* is the Burgers vector.

The stress required to force the dislocation between precipitates is expressed by

$$\tau = \frac{Gb}{\lambda} \tag{22}$$

where λ is the length between precipitates.

These equations mean that the stress increases with increasing ε, r, and f, and decreasing λ. In the observation area, that is, the center of a specimen compressed at 950 °C and a strain rate of 25 s^{-1}, the nanosized γ'' phases with circular and elongated disk shapes, and the microsized δ phases with block shapes can be observed throughout the microstructure, as shown in Figure 12. Since the γ'' phases are the main reinforcing factor coherent with the matrix [24], and the δ phases precipitate at grain boundaries [39,40] and contribute not to precipitation hardening but to grain boundary strengthening [41], the increase in the plastic modulus F_1 at 950 °C may be greater than that at 1050 °C. In addition, an unstable state is formed around the precipitates such as the γ'' phases owing to piled-up dislocations caused by deformation and DRX or SIDT occurs as it functions as a nucleation site based on this energy [42–44], decreasing ε_c. Therefore, the dynamically precipitated δ phases deformed at 1050 °C and γ'' phases deformed at 950 °C might affect the increase in F_1 and the decrease in ε_c, reducing the accuracy of regression in terms of, for example, the strain rate sensitivity m and the temperature sensitivity $A1$. Further research would be necessary to obtain a more accurate generalized flow curve by considering these effects. A schematic illustration of the change of the PTT diagram during hot working at high strain rates is represented in Figure 13.

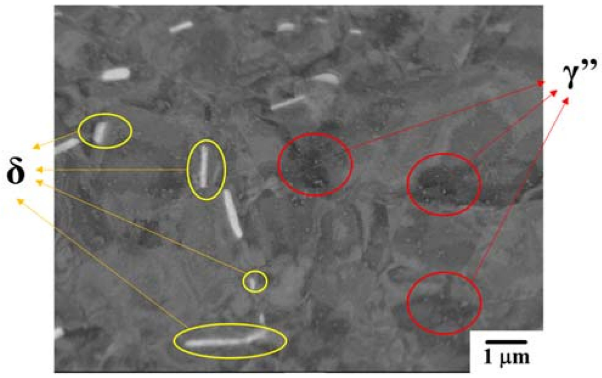

Figure 12. Microstructure with precipitated δ and γ'' phases in superalloy 718 after hot compression at a 67% height reduction, a deformation temperature of 950 °C, and a strain rate of 25 s^{-1}.

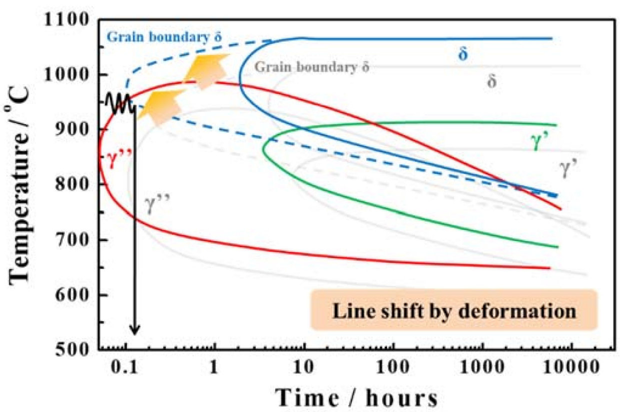

Figure 13. Schematic illustration of shift of PTT diagram during hot working at deformation temperature of 950 °C and high strain rates.

4. Conclusions

Hot compression tests in superalloy 718 with IA at deformation temperatures from 850 to 1100 °C, a 67% height reduction, and strain rates of 1, 10, and 25 s^{-1} were performed to obtain the uniaxial flow stress and its generalized equation considering the effects of DRX and SIDP. The main research results are summarized as follows:

1. A flow curve obtained from experimental results at a deformation temperature of 950 °C and a strain rate of 1 s^{-1} shows strong DRX behavior. On the other hand, a flow curve obtained from IA results at a deformation temperature of 950 °C and a strain rate of 1 s^{-1} shows weak DRX behavior and complex dynamic events such as DRV and DRX. This might be attributed to the flow curve obtained from the experimental results, including the effects of internal–external heat transfer, friction, and heat generated by hot working, leading to heterogeneous deformation. From IA results, a uniaxial flow stress can be attained to remove those effects.
2. The dynamically precipitated δ phases deformed at 1050 °C and γ'' phases deformed at 950 °C might affect the increase in the plastic modulus F_1 and the decrease in the critical strain ε_c, deteriorating the accuracy of regression in terms of, for example, the strain rate sensitivity m and the temperature sensitivity A.
3. A high-precision constitutive equation for the generalized flow curve in superalloy 718 has been achieved by using the temperature sensitivity $A2$ obtained from the relationship between $\ln(F_3)$ and $10^3(1/T–1/T^*)$, instead of the temperature sensitivity $A1$ obtained from the relationship between $\ln\left(F_1'\dot{\varepsilon}^{m_0-m}\right)$ and $10^3(1/T–1/T^*)$, which is affected by the plastic modulus F_1 and the critical strain ε_c.

Author Contributions: Investigation, H.-W.P. and S.K.; inverse analysis, H.-W.P. and K.K.; methodology, H.-W.P., S.K., K.K., A.Y. and J.Y.; writing—original draft, H.-W.P.; writing—review and editing, K.K., A.Y. and J.Y.; supervision, J.Y. All authors have read and agreed to the published version of the manuscript.

Funding: This work was supported by the Council for Science, Technology and Innovation (CSTI), Cross-ministerial Strategic Innovation Promotion Program (SIP) in Japan, "Structural Materials for Innovation" (Unit No. B21, Development of Innovative Forging Process Technology and Construction of Material/Process Database with the Largescale and Precise Forging Simulator).

Institutional Review Board Statement: Not applicable.

Informed Consent Statement: Not applicable.

Data Availability Statement: The data presented in this study are available on request from the corresponding author.

Conflicts of Interest: The authors declare no conflict of interest.

References

1. The Japan Research and Development Center for Metals. *JRCM NEWS*, March 2007; 2–6. Available online: http://www.jrcm.or.jp/jrcmnews/0703jn245.pdf(accessed on 5 July 2021).
2. Thamboo, S.V.; Schwant, R.C.; Yang, L.; Jackman, L.A.; Bond, B.J.; Kennedy, R.L. Large diameter 718 ingots for land-based gas turbines. In *Superalloys 718, 625, 706 and Various Derivatives*; Loria, E.A., Ed.; TMS: Warrendale, PA, USA, 2001; pp. 57–70.
3. Uginet, J.F.; Jackson, J.J. Alloy 718 forging development for large land-based gas turbine. In *Superalloys 718, 625, 706 and Derivatives*; Loria, E.A., Ed.; TMS: Warrendale, PA, USA, 2005; pp. 57–67.
4. Chamanfar, A.; Sarrat, L.; Jahazi, M.; Asadi, M.; Weck, A.; Koul, A.K. Microstructural characteristics of forged and heat treated Inconel-718 disks. *Mater. Des.* **2013**, *52*, 791–800. [CrossRef]
5. Alabort, E.; Reed, R.C.; Barba, D. Combined modelling and miniaturised characterisation of high-temperature forging in a nickel-based superalloy. *Mater. Des.* **2018**, *160*, 683–697. [CrossRef]
6. Tan, Y.B.; Ma, Y.H.; Zhao, F. Hot deformation behavior and constitutive modeling of fine grained Inconel 718 superalloy. *J. Alloys Compd.* **2017**, *716*, 65–72. [CrossRef]
7. Azarbarmas, M.; Aghaie-Khafri, M.; Cabrera, J.M.; Calvo, J. Microstructural evolution and constitutive equations of Inconel 718 alloy under quasi-static and quasi-dynamic conditions. *Mater. Des.* **2016**, *94*, 28–38. [CrossRef]

8. Chen, F.; Liu, J.; Ou, H.; Lu, B.; Cui, Z.; Long, H. Flow characteristics and intrinsic workability of IN718 superalloy. *Mater. Sci. Eng. A* **2015**, *642*, 279–287. [CrossRef]
9. Gujrati, R.; Gupta, C.; Jha, J.S.; Mishra, S.; Alankar, A. Understanding activation energy of dynamic recrystallization in Inconel 718. *Mater. Sci. Eng. A* **2019**, *744*, 638–651. [CrossRef]
10. Tang, X.; Wang, B.; Huo, Y.; Ma, W.; Zhou, J.; Ji, H.; Fu, X. Unified modeling of flow behavior and microstructure evolution in hot forming of a Ni-based superalloy. *Mater. Sci. Eng. A* **2016**, *662*, 54–64. [CrossRef]
11. Yanagida, A.; Liu, J.; Yanagimoto, J. Flow curve determination for metal under dynamic recrystallization using inverse analysis. *Mater. Trans.* **2003**, *44*, 2303–2310. [CrossRef]
12. Yanagida, A.; Yanagimoto, J. Regression method of determining generalized description of flow curve of steel under dynamic recrystallization. *ISIJ Int.* **2005**, *45*, 858–866. [CrossRef]
13. Soltanpour, M.; Yanagimoto, J. Material data for the kinetics of microstructure evolution of Cr–Mo–V steel in hot forming. *J. Mater. Proc. Technol.* **2012**, *212*, 417–426. [CrossRef]
14. Meng, Y.; Lin, J.Y.; Yanagida, A.; Yanagimoto, J. Modeling static and dynamic kinetics of microstructural evolution in hot deformation of Fe–0.15C–0.2Si–1.4Mn–0.03Nb alloy. *Steel Res. Int.* **2017**, *88*, 1700036. [CrossRef]
15. Park, H.W.; Kim, K.; Park, H.W.; Ding, S.; Yanagimoto, J. Formulation of a generalized flow curve for 0.2% carbon steel under high-speed hot forming conditions by a regression method. *ISIJ Int.* **2020**, *60*, 2896–2904. [CrossRef]
16. Dupin, E.; Yanagida, A.; Yanagimoto, J. Modeling static and dynamic kinetics of microstructure evolution in type 316 stainless steel. *Steel Res. Int.* **2014**, *85*, 1099–1108. [CrossRef]
17. Kim, K.; Park, H.W.; Ding, S.; Park, H.W.; Yanagimoto, J. Flow stress of duplex stainless steel by inverse analysis with dynamic recovery and recrystallization model. *ISIJ Int.* **2021**, *61*, 280–291. [CrossRef]
18. Ding, S.; Khan, S.A.; Yanagimoto, J. Constitutive descriptions and microstructure evolution of extruded A5083 aluminum alloy during hot compression. *Mater. Sci. Eng. A* **2018**, *728*, 133–143. [CrossRef]
19. Ding, S.; Khan, S.A.; Yanagimoto, J. Flow behavior and dynamic recrystallization mechanism of A5083 aluminum alloys with different initial microstructures during hot compression. *Mater. Sci. Eng. A* **2020**, *787*, 139522. [CrossRef]
20. Horikoshi, S.; Yanagida, A.; Yanagimoto, J. Uniform hot compression of nickel-based superalloy 720Li under isothermal and low friction conditions. *ISIJ Int.* **2020**, *60*, 2905–2916. [CrossRef]
21. Thomas, A.; El-Wahabi, M.; Cabrera, J.M.; Prado, J.M. High temperature deformation of Inconel 718. *J. Mater. Proc. Technol.* **2006**, *177*, 469–472. [CrossRef]
22. Desvallees, Y.; Bouzidi, M.; Bois, F.; Beaude, N. Delta phase in INCONEL 718: Mechanical properties and forging process requirements. In *Superalloys 718, 625, 706 and Various Derivatives*; Loria, E.A., Ed.; TMS: Warrendale, PA, USA, 1994; pp. 281–291.
23. Azadian, S.; Wei, L.Y.; Warren, R. Delta phase precipitation in Inconel 718. *Mater. Charact.* **2004**, *53*, 7–16. [CrossRef]
24. Slama, C.; Abdellaoui, M. Structural characterization of the aged Inconel 718. *J. Alloys Compd.* **2000**, *306*, 277–284. [CrossRef]
25. Kulawik, K.; Buffat, P.A.; Kruk, A.; Wusatowska-Sarnek, A.M.; Czyrska-Filemonowicz, A. Imaging and characterization of γ' and γ'' nanoparticles in Inconel 718 by EDX elemental mapping and FIB–SEM tomography. *Mater. Charact.* **2015**, *100*, 74–80. [CrossRef]
26. Calvo, J.; Penalva, M.; Cabrera, J.M. Characterization of strain-induced precipitation in Inconel 718 superalloy. *J. Mater. Eng. Perform.* **2016**, *25*, 3409–3417. [CrossRef]
27. Nowotnik, A.; Sieniawski, J.; Mrówka-Nowotnik, G. Identification of dynamically precipitated phases in hot-working Inconel 718 alloy. *J. Achiev. Mater. Manuf. Eng.* **2008**, *31*, 275–280.
28. Nowotnik, A. The influence of hot-deformation parameters on the mechanical properties and precipitation process in nickel based superalloy. In *Superalloys 2008*; Reed, R.C., Green, K.A., Caron, P., Gabb, T.P., Fahrmann, M.G., Huron, E.S., Woodard, S.A., Eds.; TMS: Warrendale, PA, USA, 2008; pp. 709–718.
29. Chen, S.; Chen, K.; Peng, G.; Chen, X.; Ceng, Q. Effect of heat treatment on hot deformation behavior and microstructure evolution of 7085 aluminum alloy. *J. Alloys Compd.* **2012**, *537*, 338–345. [CrossRef]
30. Ebrahimi, G.R.; Momeni, A.; Kazemi, S.; Alinejad, H. Flow curves, dynamic recrystallization and precipitation in a medium carbon low alloy steel. *Vacuum* **2017**, *142*, 135–145. [CrossRef]
31. Mirzaee, M.; Keshmiri, H.; Ebrahimi, G.R.; Momeni, A. Dynamic recrystallization and precipitation in low carbon low alloy steel 26NiCrMoV 14-5. *Mater. Sci. Eng. A* **2012**, *551*, 25–31. [CrossRef]
32. Sellars, C.M.; McTegart, W.J. On the mechanism of hot deformation. *Acta Metall.* **1966**, *14*, 1136–1138. [CrossRef]
33. Cheng, L.; Xue, X.; Tang, B.; Liu, D.; Li, J.; Kou, H.; Li, J. Deformation behavior of hot-rolled IN718 superalloy under plane strain compression at elevated temperature. *Mater. Sci. Eng. A* **2014**, *606*, 24–30. [CrossRef]
34. Wang, Y.; Shao, W.Z.; Zhen, L.; Zhang, B.Y. Hot deformation behavior of delta-processed superalloy 718. *Mater. Sci. Eng. A* **2011**, *528*, 3218–3227. [CrossRef]
35. Song, R.; Ponge, D.; Raabe, D.; Speer, J.G.; Matlock, D.K. Overview of processing, microstructure and mechanical properties of ultrafine grained bcc steels. *Mater. Sci. Eng. A* **2006**, *441*, 1–17. [CrossRef]
36. Park, H.W.; Yanagimoto, J. Formation process and mechanical properties of 0.2% carbon steel with bimodal microstructures subjected to heavy-reduction single-pass hot/warm compression. *Mater. Sci. Eng. A* **2013**, *567*, 29–37. [CrossRef]

37. Park, H.W.; Shimojima, K.; Sugiyama, S.; Komine, H.; Yanagimoto, J. Microstructural evolution and formation mechanism of bimodal structure of 0.2% carbon steel subjected to the heavy-reduction controlled rolling process. *Mater. Sci. Eng. A* **2015**, *624*, 203–212. [CrossRef]
38. Dieter, G.E. *Mechanical Metallurgy*, 3rd ed.; McGraw-Hill: New York, NY, USA, 1986.
39. Cao, G.H.; Sun, T.Y.; Wang, C.H.; Li, X.; Liu, M.; Zhang, Z.X.; Hu, P.F.; Russell, A.M.; Schneider, R.; Gerthsen, D.; et al. Investigations of γ', γ'' and δ precipitates in heat-treated Inconel 718 alloy fabricated by selective laser melting. *Mater. Charact.* **2018**, *136*, 398–406. [CrossRef]
40. Sundararaman, M.; Mukhopadhyay, P.; Banerjee, S. Precipitation of the δ-Ni_3Nb phase in two nickel base superalloys. *Metall. Mater. Trans. A* **1988**, *19*, 453–465. [CrossRef]
41. Hall, R.C. The Metallurgy of Alloy 718. *J. Basic Eng.* **1967**, *89*, 511–516. [CrossRef]
42. Huang, K.; Logé, R.E. A review on dynamic recrystallization phenomena in metallic materials. *Mater. Des.* **2016**, *111*, 548–574. [CrossRef]
43. Park, H.W.; Yanagimoto, J. Effect of carbon content on formation of bimodal microstructure and mechanical properties of low-carbon steels subjected to heavy-reduction single-pass hot/warm deformation. *Mater. Sci. Eng. A* **2014**, *607*, 542–550. [CrossRef]
44. Lee, S.H.; Na, H.S.; Kim, B.H.; Kim, D.J.; Kang, C.Y. Effect of niobium on the ferrite continuous-cooling-transformation (CCT) curve of ultrahigh-thickness Cr-Mo steel. *Metall. Mater. Trans. A* **2013**, *44*, 2523–2532. [CrossRef]